Available online at www.sciencedirect.com
SCIENCE DIRECT®
Journal of Solid State Chemistry 176 (2003) 482–495
JOURNAL OF SOLID STATE CHEMISTRY
http://elsevier.com/locate/jssc

Density functional application to strongly correlated electron systems

H. Eschrig,* K. Koepernik, and I. Chaplygin

Leibniz-Institute für Festkörper & Werkstofforschung (IFW) Dresden, P.O. Box 27 00 16, D-01171 Dresden, Germany

Received 19 January 2003; received in revised form 2 May 2003; accepted 6 May 2003

This paper is dedicated to Walter Kohn on the occasion of his 80th birthday in March 2003

Abstract

The local spin density approximation plus onsite Coulomb repulsion approach (LSDA + U) to density functional theory is carefully reanalyzed. Its possible link to single-particle Green's function theory is occasionally discussed. A simple and elegant derivation of the important sum rules for the on-site interaction matrix elements linking them to the values of U and J is presented. All necessary expressions for an implementation of LSDA + U into a non-orthogonal basis solver for the Kohn–Sham equations are given, and implementation into the full-potential local-orbital solver (Phys. Rev. B 59 (1999) 1743) is made. Results of application to several planar cuprate structures are reported in detail and conclusions on the interpretation of the physics of the electronic structure of the cuprates are drawn.

Keywords: Electronic structure theory; Correlated electron systems; Cuprates

1. Introduction

Density functional theory (DFT) based on the variational principle by Hohenberg and Kohn [1] has nowadays a rigorous mathematical basis, mainly due to work by Lieb [2]. As a theory for (chosen) ground state properties of a many-particle system, it holds true for any Coulomb quantum system with arbitrarily strong correlations in the ground state. All hampering representability problems of the early time are gone (see for instance [3]). However, the central quantity, the universal density functional is not known, only its existence can be proved, and we have no fully systematic access by approximations. Hence, so far (and very likely also in future) we have to model it and to probe the models by comparison to phenomenology. This situation is not principally different from other many-particle approaches where either models of sufficiently simple Hamiltonians are used (in quantum field theory) or the wave function is modeled (for instance in Hartree–Fock or Gutzwiller approaches).

The situation is even less satisfactory in solid-state theory, if the focus is on the excitation spectra instead on the ground state, because in most cases the spectrum of the many-body Hamiltonian has no separate physical relevance at all except for its formal use in theoretical expressions for the partition function. Instead, what is measured are the spectra of various quasistationary excitations, defined from few-particle Green's functions, the self-energy parts of which, besides being energy-dependent non-linear integral operators, are also density functionals.

Although this is not a principal restriction of DFT, the models in use so far (local (spin) density approximation, L(S)DA, in the following the acronym LSDA is used for both LDA and LSDA, generalized gradient approximation, GGA, LSDA plus self-interaction correction, SIC, LSDA plus onsite Coulomb repulsion, LSDA + U, …) are subject to the adiabatic approximation for the electron–lattice interaction.

DFT in the Kohn–Sham (KS) approach to solids yields a KS band structure, which as such does also not have a direct physical meaning. Instead, the quasiparticle band structure of Bloch electrons is obtained from the self-energy of the electron Green's function. It has become common use to speak of weak correlations, if in the vicinity of the Fermi level the LSDA KS potential and the electron self-energy are not very different. This does by no means imply that the correlation energy

*Corresponding author: Fax: +49(0)351-4659-500.
E-mail address: h.eschrig@ifw-dresden.de (H. Eschrig).

0022-4596/03/$ - see front matter © 2003 Elsevier Inc. All rights reserved.
doi:10.1016/S0022-4596(03)00274-3

itself, defined as the difference between the true total energy and the Hartree–Fock energy, is small or much smaller than in strongly correlated systems (where the LSDA KS potential differs strongly from the electron self-energy, the latter often jumps as a function of energy at the Fermi level). It is a general experience that in the latter cases also the ground state properties, or certain ground state properties, are much worse reproduced by the LSDA than in weakly correlated cases (in the above definition).

This paper deals with strongly correlated systems treated by means of the LSDA + U approach. May be the first precursor of an LSDA + U calculation (at that time not fully self-consistent) was the treatment of 4f-electrons by Herbst et al. [4]. A first fully self-consistent calculation of values of the Hubbard U was performed by Dederichs et al. [5] for the 4f-states of Ce by applying the Korringa–Kohn–Rostoker solver of the KS equations to a constraint impurity problem. An early similar approach to U for NiO by Norman and Freeman [6] used the augmented plane wave (APW) solver in a super-cell formulation. For the further development of this subject see [7].

Pickett and Wang [8] and Hybertsen and Louie [9] based the so-called GW-approximation for the electron self-energy of semi-conductors and insulators on LDA results for the density and KS bands as a starting approximation for the GW-approach. In these cases the main difference between the LDA KS potential and the self-energy is a jump of the latter, constant in $\boldsymbol{r}$-space at the Fermi level [10] (scissors operation). This is still considered a weakly correlated case, but these were the first estimates of the self-energy of an inhomogeneous situation as a density functional.

A systematic incorporation of the Hubbard U-potential into the DFT model functionals started with two papers by Anisimov et al. [11,12]. While it was proposed in [11] to model the total spin dependence by the U-functional and to treat the spin-independent functional by the LDA, in [12] the orbital polarization part (m-dependent occupation of local orbitals) was treated by the U-functional and the isotropic (in $\boldsymbol{r}$-space) part of the spin density was treated in LSDA. This has the advantage that spin polarization effects can be treated more generally, not only in the strongly correlated orbitals. However, this version, later on called 'around the mean field', AMF, by Czyżyk and Sawatzky [13], gives nearly nothing for a half-filled fully spin polarized shell as in Mn^{2+} or in Gd. Therefore, aiming mainly at reproducing the photoemission spectra (which essentially means modeling the electron self-energy rather than the KS potential), an alternative U-functional was introduced in [13] and called the 'atomic limit' version, AL. This version which roughly shifts unoccupied orbital energies upward by $U/2$ and occupied orbital energies downward by $U/2$ independent of the shell filling (even for filled and empty shells), has been widely used since. For a survey see [14].

It has to be confessed that all LSDA + U models up to now depend on the basis used for the KS solver. Most results are obtained so far with an linearized muffin tin orbital (LMTO) implementation. For a recent APW implementation see [15].

In this paper, in Section 2, a full-potential local-orbital (FPLO) implementation is described. FPLO [16] is a high precision high efficiency KS solver which uses a minimum basis (and hence is fast) containing only local basis functions which are optimized in both a numerical and chemical sense. (It competes in accuracy with well converged full-potential APW.) After a short outline how U is integrated into DFT, the correlated orbitals used in the FPLO implementation are introduced. Since literature statements [13] say that the most important sum rules for the interaction matrix elements (screened Slater integrals) of those orbitals are cumbersome to verify, a very simple and elegant derivation is given here. After the necessary analysis of the orbital occupation matrix for the non-orthogonal basis of FPLO and the introduction of the AMF and AL functionals in the FPLO implementation, explicit expressions for the U-potential and for the total energy are given as they are coded in FPLO LSDA + U. In Section 3, new applications to cuprate structures, the 'infinite layer' compound $CaCuO_2$, the undoped single-layer compound $Sr_2CuO_2Cl_2$ and the bilayer high-temperature superconductor $Bi_2Sr_2CaCu_2O_8$ are considered and the results are compared to both magnetic ground state properties and photoemission spectra. A short summary is given in Section 4.

2. The FPLO implementation of the LSDA + U approach

The underlying frame of the LSDA + U approach is the Hohenberg–Kohn variational principle,

$$E[\check{v},N]=\min_{\check{n}}\left\{H[\check{n}]+\sum_{ss'}\int \mathrm{d}^3r\, v_{ss'}(\boldsymbol{r})n_{s's}(\boldsymbol{r})\,\middle|\,\sum_{s}\int \mathrm{d}^3r\, n_{ss}(\boldsymbol{r})=N\right\} \tag{1}$$

for the ground state energy E and spin density $\check{n}=(n_{ss'})$ of N electrons in an external spin-dependent potential $\check{v}$,

$$\sum_{ss'}\int \mathrm{d}^3r\, v_{ss'}(\boldsymbol{r})n_{s's}(\boldsymbol{r})=\int \mathrm{d}^3r\,(vn-\boldsymbol{B}\cdot\boldsymbol{m}), \tag{2}$$

which holds true in any case of arbitrarily strong correlation. It is based on many-particle quantum theory by rigorous mathematics [3]. Of course, the density functional $H[\check{n}]$ is unknown.

The generalized Kohn–Sham modeling of this functional is by parameterizing the variational spin density

by new variational parameters: the Kohn–Sham orbitals $\phi_i(\boldsymbol{r}, s)$ and orbital occupation numbers n_i,

$$n_{ss'}(\boldsymbol{r}) = \sum_i \phi_i(\boldsymbol{r}s) n_i \phi_i^*(\boldsymbol{r}s'), \quad \langle \phi_i | \phi_j \rangle = \delta_{ij},$$
$$0 \leqslant n_i \leqslant 1, \quad \sum_i n_i = N, \tag{3}$$

and by splitting the density functional into an orbital variation expression $K[\check{n}]$ and a (possibly generalized by gradient terms) local density expression $L[\check{n}]$:

$$H[\check{n}] = K[\check{n}] + L[\check{n}],$$
$$K[\check{n}] = \min_{\{\phi_i, n_i\}} \left\{ k[\phi_i, n_i] \middle| \sum_i \phi_i n_i \phi_i^* = \check{n} \right\},$$
$$L[\check{n}] = \int \mathrm{d}^3 r \, n(\boldsymbol{r}) l(n_{ss'}(\boldsymbol{r}), \boldsymbol{\nabla} n, \ldots). \tag{4}$$

This puts the Hohenberg–Kohn variational principle into the Kohn–Sham form

$$E[\check{v}, N] = \min_{\{\phi_i, n_i\}} \left\{ k[\phi_i, n_i] + L\left[\sum_i \phi_i n_i \phi_i^*\right] + \sum_i n_i \langle \phi_i | \check{v} | \phi_i \rangle \middle| \langle \phi_i | \phi_j \rangle = \delta_{ij}, 0 \leqslant n_i \leqslant 1, \sum_i n_i = N \right\}. \tag{5}$$

While for the L-functional LSDA or GGA models are in use, k is modeled by LSDA or LSDA + SIC or LSDA + U. Variation of ϕ_i^* yields the generalized Kohn–Sham equation,

$$\frac{1}{n_i} \frac{\delta k}{\delta \phi^*} + (\check{v}^L + \check{v}) \phi_i = \phi_i \varepsilon_i, \quad v^L_{ss'} = \frac{\delta L}{\delta n_{s's}}, \tag{6}$$

and variation of the n_i yields the common aufbau principle which holds true for all model variants within this frame and which says that the ground state density is obtained by occupying the N orbitals with the lowest ε_i.

The variants of the LSDA + U model correspond to $k = t + e^H + e^U$,

$$t + e^H = \sum_i n_i \langle \phi_i | \hat{t} | \phi_i \rangle + \frac{1}{2} \sum_{ij} n_i n_j \langle \phi_i \phi_j | r_{ij}^{-1} | \phi_i \phi_j \rangle, \tag{7}$$

where e^U is expressed through projection onto correlated local orbitals $|\boldsymbol{R}\mu\sigma)$ centered at site (or in the unit cell) $\boldsymbol{R}$ and with orbital and spin quantum numbers μ and σ. The projection is given by a local orbital occupation number $\tilde{n}_{\mu\sigma}$ which depends on the variational quantities ϕ_i, n_i:

$$e^U = e^U(\tilde{n}_{\mu\sigma}[\phi_i, n_i]), \quad \frac{1}{n_i} \frac{\delta}{\delta \phi_i^*} e_U = \sum_{\boldsymbol{R}\mu\sigma} \frac{\partial e^U}{\partial \tilde{n}_{\mu\sigma}} \frac{1}{n_i} \frac{\delta \tilde{n}_{\mu\sigma}}{\delta \phi_i^*}. \tag{8}$$

The functional derivative on the r.h.s. of the last expression yields the projection while the partial derivative defines the orbital and spin-dependent U-potential: $v^U_{\mu\sigma} = \partial e^U / \partial \tilde{n}_{\mu\sigma}$. It is crucial for fitting the models in use into the general Hohenberg–Kohn–Sham frame that the correlated orbitals themselves as well as the actual value of U are understood fixed and not variational although they may be context dependent. They may be thought of defining a location, relevant in a given context, in the variational functional space and a functional contribution from that location.

2.1. Correlated orbitals

In the so-called rotationally invariant LSDA + U approach the correlated local orbitals are assumed to be angular momentum eigenstates centered at $\boldsymbol{R}$, say, with predefined orbital and spin momentum quantization axes (which both need not be the same)

$$|\boldsymbol{R}_i m_i \sigma_i), \quad m_i = -l_i, \ldots, l_i, \quad \sigma_i = \uparrow, \downarrow. \tag{9}$$

Only one-site matrix elements, $\boldsymbol{R}_1 = \boldsymbol{R}_2 = \boldsymbol{R}_3 = \boldsymbol{R}_4$, are considered:

$$(m_1 m_2 | \tilde{w} | m_3 m_4), \quad \tilde{w} \approx \tilde{w}(|\boldsymbol{r} - \boldsymbol{r}'|), \quad \sigma_1 = \sigma_3, \quad \sigma_2 = \sigma_4. \tag{10}$$

The rotational invariance refers to the screened electron–electron interaction, $\tilde{w}$, which is of course an approximation as regards the screening. As a consequence, the SO_3 transformation properties of the matrix elements are

$$(m_1 m_2 | \tilde{w} | m_3 m_4) = \sum_{m'_1 m'_2 m'_3 m'_4} U^\dagger_{m_1 m'_1}(\hat{O}) U^\dagger_{m_2 m'_2}(\hat{O}) * (m'_1 m'_2 | \tilde{w} | m'_3 m'_4) U_{m'_3 m_3}(\hat{O}) U_{m'_4 m_4}(\hat{O}), \tag{11}$$

where $\hat{O}$ is any rotation of the $\boldsymbol{r}$-space and the U-matrices (not to be confused with the Coulomb integral U) yield the relevant SO_3 representation:

$$U^\dagger(\hat{O}) U(\hat{O}) = 1 = U(\hat{O}) U^\dagger(\hat{O}),$$
$$\int \mathrm{d}\hat{O} \, U_{m_1 m_2}(\hat{O}) U^\dagger_{m_3 m_4}(\hat{O}) = \frac{1}{2l+1} \delta_{m_1 m_4} \delta_{m_2 m_3}. \tag{12}$$

In the last orthogonality relation, $\mathrm{d}\hat{O}$ is Haar's measure of the SO_3, $\int \mathrm{d}\hat{O} = 1$.

These fundamental representation properties allow for a very simple and elegant derivation of the important sum rules for the matrix elements: Use unitarity of U

and integrate over $\mathrm{d}\hat{O}$ to obtain

$$\begin{aligned}
&\sum_{m_1} (m_1 m_2|\tilde{w}|m_1 m_4) \\
&\quad = \sum_{m_1} \sum_{m'_1 m'_2 m'_3 m'_4} U^{\dagger}_{m_1 m'_1}(\hat{O}) U^{\dagger}_{m_2 m'_2}(\hat{O}) (m'_1 m'_2|\tilde{w}|m'_3 m'_4) \\
&\qquad \cdot U_{m'_3 m_1}(\hat{O}) U_{m'_4 m_4}(\hat{O}) \\
&\quad = \sum_{m'_1 m'_2 m'_3 m'_4} \delta_{m'_1 m'_3} U^{\dagger}_{m_2 m'_2}(\hat{O}) (m'_1 m'_2|\tilde{w}|m'_3 m'_4) U_{m'_4 m_4}(\hat{O}) \\
&\quad = \frac{1}{2l+1} \sum_{m'_1 m'_2 m'_4} (m'_1 m'_2|\tilde{w}|m'_1 m'_4) \delta_{m_2 m_4} \delta_{m'_2 m'_4} \\
&\quad = \frac{\delta_{m_2 m_4}}{2l+1} \sum_{m'_1 m'_2} (m'_1 m'_2|\tilde{w}|m'_1 m'_2) \\
&\quad = \delta_{m_2 m_4} (2l+1) U. \qquad (13)
\end{aligned}$$

The last equation is the definition of the Coulomb integral U. In the same manner,

$$\begin{aligned}
&\sum_{m_1} (m_1 m_2|\tilde{w}|m_3 m_1) \\
&\quad = \frac{\delta_{m_2 m_3}}{2l+1} \sum_{m'_1 m'_2} (m'_1 m'_2|\tilde{w}|m'_2 m'_1) \\
&\quad = \delta_{m_2 m_3} (U + 2lJ) \qquad (14)
\end{aligned}$$

is obtained which additionally defines the exchange integral J. The first result (13) is intuitively obvious: after summation over m_1 and integration over $\boldsymbol{r}$ in the matrix element, no angular dependence with respect to $\boldsymbol{r}'$ is left except the orthogonality $(m_2|m_4) = \delta_{m_2 m_4}$. The second result (14) is less obvious but nevertheless true.

Expansion of the interaction function into spherical harmonics,

$$\begin{aligned}
\tilde{w}(|\boldsymbol{r}_1 - \boldsymbol{r}_2|) &= \tilde{w}((r_1^2 + r_2^2 - 2 r_1 r_2 \cos\theta)^{1/2}) \\
&= \sum_{l=0}^{\infty} \tilde{w}_l(r_1, r_2) P_l(\cos\theta) \\
&= \sum_{l=0}^{\infty} \tilde{w}_l(r_1, r_2) \frac{4\pi}{2l+1} \\
&\quad \times \sum_{m=-l}^{l} Y_{lm}(\hat{\boldsymbol{r}}_1) Y^*_{lm}(\hat{\boldsymbol{r}}_2) \qquad (15)
\end{aligned}$$

leads to Slater's analysis

$$(m_1 m_2|\tilde{w}|m_3 m_4) = \sum_{l=0}^{2l_i} \tilde{F}_l a_l(m_1 m_2 m_3 m_4),$$

$$\begin{aligned}
\tilde{F}_l &= \int\int_0^{\infty} dr_1 dr_2 \, (r_1 R_i(r_1))^2 (r_2 R_i(r_2))^2 \tilde{w}_l(r_1, r_2) \\
&\approx \int\int_0^{\infty} dr_1 dr_2 \, (r_1 R_i(r_1))^2 (r_2 R_i(r_2))^2 \frac{r_<^l}{r_>^{l+1}} \\
&\quad \text{for } l > 0, \qquad (16)
\end{aligned}$$

$$\begin{aligned}
a_l(m_1 m_2 m_3 m_4) = &\frac{4\pi}{2l+1} \sum_{m=-l}^{l} (Y_{l_i m_1}|Y_{lm}|Y_{l_i m_3}) \\
&\times (Y_{l_i m_4}|Y_{lm}|Y_{l_i m_2})^*.
\end{aligned}$$

Here, l_i is the angular momentum of the considered shell, and the second line for $\tilde{F}_l$ holds for the unscreened Coulomb interaction which for $l > 0$ is a reasonable approximation since intraatomic screening is effective only for the s-component of the interaction.

Now, from $\sum_m Y_{lm}(\boldsymbol{r}) Y^*_{lm}(\boldsymbol{r}) = P_l(1)(2l+1)/4\pi$ and

$$\begin{aligned}
&\sum_{m_1} a_l(m_1 m_2 m_1 m_2) \\
&\quad = \frac{4\pi}{2l+1} \left[\sum_{m_1} (Y_{l_i m_1}|Y_{l0}|Y_{l_i m_1}) \right] (Y_{l_i m_2}|Y_{l0}|Y_{l_i m_2})^* \\
&\quad = \sqrt{4\pi} \frac{2l_i+1}{2l+1} \delta_{l0} (Y_{l_i m_2}|Y_{l0}|Y_{l_i m_2})^* = (2l_i+1)\delta_{l0}
\end{aligned}$$

it follows immediately that

$$U = \tilde{F}_0. \qquad (17)$$

Furthermore,

$$\begin{aligned}
&\sum_{m_1 m_2} a_l(m_1 m_2 m_2 m_1) \\
&\quad = \frac{4\pi}{2l+1} \sum_{\substack{m_1 m_2 \\ m}} (Y_{l_i m_1}|Y_{lm}|Y_{l_i m_2}) (Y_{l_i m_2}|Y^*_{lm}|Y_{l_i m_1}) \\
&\quad = \frac{4\pi}{2l+1} \int\int \mathrm{d}\Omega_1 \, \mathrm{d}\Omega_2 \left(\sum_{m_1} Y_{l_i m_1}(\boldsymbol{r}_2) Y^*_{l_i m_1}(\boldsymbol{r}_1) \right) \\
&\qquad * \left(\sum_{m_2} Y_{l_i m_2}(\boldsymbol{r}_1) Y^*_{l_i m_2}(\boldsymbol{r}_2) \right) \left(\sum_{m} Y_{lm}(\boldsymbol{r}_1) Y^*_{lm}(\boldsymbol{r}_2) \right) \\
&\quad = \frac{(2l_i+1)^2}{(4\pi)^2} \int\int \mathrm{d}\Omega_1 \, \mathrm{d}\Omega_2 \, [P_{l_i}(\cos\theta_{12})]^2 P_l(\cos\theta_{12}) \\
&\quad = \frac{(2l_i+1)^2}{4\pi} \int \mathrm{d}\Omega \, [P_{l_i}(\cos\theta)]^2 P_l(\cos\theta) \\
&\quad = (2l_i+1)^2 \begin{pmatrix} l_i & l & l_i \\ 0 & 0 & 0 \end{pmatrix}^2
\end{aligned}$$

and hence

$$\begin{aligned}
\sum_{m_1 m_2} (m_1 m_2|\tilde{w}|m_2 m_1) &= (2l_i+1)^2 \sum_{l=0}^{2l_i} \tilde{F}_l \begin{pmatrix} l_i & l & l_i \\ 0 & 0 & 0 \end{pmatrix}^2 \\
&= (2l_i+1)(U + 2l_i J). \qquad (18)
\end{aligned}$$

Eqs. (17) and (18) relate the Coulomb and exchange integrals U and J to Slater's (screened) integrals $\tilde{F}_l$.

Recall, however, that the whole analysis presupposes the isotropy of screening which could be questioned at least in cases of strong directional covalency.

2.2. The orbital occupation matrix

The variants of the LSDA + U model are all depending on the basis set of the solver of the Kohn–Sham equations. There are a few subtleties in this game which never have been discussed in the literature. Here, a non-orthogonal local basis implementation [16] of the solver will be used, since a local orbital representation is mandatory for considering strong correlations. Non-orthogonality of the basis is rather the rule than the exception for high precision solvers. For an LMTO solver see [17], for an LAPW solver see [15].

Consider Kohn–Sham orbitals $|k\rangle = |\phi_k\rangle$ and orbital occupation numbers n_k as previously; they need not be eigenstates of spin. Let $\{|l)\}$ be a possibly non-orthogonal basis for Kohn–Sham orbitals: $|k\rangle = \sum_l |l)c_{lk}, S_{ll'} = (l|l')$. (Systematically, brackets are used for the Kohn–Sham orbitals and parentheses for the local basis orbitals.) For an orthogonal projection onto those basis orbitals the contragradient basis $|l\} = \sum_{l'} |l')(S^{-1})_{l'l}, \{l|l') = \delta_{ll'}$ is needed. With its help, the occupation matrix $\tilde{n} = \tilde{n}[\phi_k, n_k]$ of correlated orbitals $|m\sigma)$ at site $\boldsymbol{R}$ in an orthogonal form is introduced as

$$\tilde{n}_{mm'\sigma} = \sum_k \sum_{ll'} (S^{-1})_{(\boldsymbol{R}m\sigma),l}(l|k\rangle n_k \langle k|l')(S^{-1})_{l',(\boldsymbol{R}m'\sigma)} = \sum_k c_{(\boldsymbol{R}m\sigma),k} n_k c^*_{(\boldsymbol{R}m'\sigma),k}. \quad (19)$$

As usually it is assumed that the spin dependence can be made site diagonal by choosing a suitable spin quantization axis. The orbital occupation matrix may be diagonalized with respect to m, m' at each lattice site $\boldsymbol{R}$ and for each spin value σ independently:

$$\tilde{n}_{mm'\sigma} = \tilde{U}^{(\sigma)}_{m\mu_\sigma} \tilde{n}_{\mu\sigma} \tilde{U}^{(\sigma)*}_{m'\mu_\sigma}. \quad (20)$$

Averages over a correlated shell of angular momentum l,

$$\tilde{n}_\sigma = \frac{1}{2l+1} \sum_\mu \tilde{n}_{\mu\sigma}, \quad \tilde{n} = \frac{1}{2}(\tilde{n}_\uparrow + \tilde{n}_\downarrow), \quad (21)$$

are used later on.

The projector in (8) is now

$$\frac{1}{n_k} \frac{\delta \tilde{n}_{\mu\sigma}}{\delta \langle k|} = \sum_{ll'} |l')(S^{-1})_{l',(\boldsymbol{R}\mu\sigma)}(S^{-1})_{(\boldsymbol{R}\mu\sigma),l}(l|k\rangle. \quad (22)$$

Naturally, in applications the correlated orbitals are assumed to form a subset of the basis orbitals, although this is not mandatory. In the FPLO scheme, the basis is adjusted in the course of iterations for solving the non-linear Kohn–Sham equations. This does not mean that the basis itself is treated as variational. Rather the relevant sector of the variational space is tracked along the way of search for the Kohn–Sham minimum. Likewise, the relevant location of correlation, that is the correlated orbitals as part of the basis, is tracked along.

2.3. The orbital polarization LSDA + U functional

This functional was introduced under the name 'around the mean field' (AMF) in Ref. [13]. It is zero if the orbitals of an atomic shell are equally occupied, hence it depends on orbital polarization. It is given by

$$l(n_{ss'}(\boldsymbol{r}), \ldots) = l_{\mathrm{LSDA}},$$

$$\begin{aligned} e^{U,\mathrm{AMF}} &= \frac{1}{2} \sum_{\boldsymbol{R}\sigma\mu\mu'} \{(\mu_\sigma \mu'_{-\sigma}|\tilde{w}|\mu_\sigma \mu'_{-\sigma})(\tilde{n}_{\mu\sigma} - \tilde{n}_\sigma)(\tilde{n}_{\mu'-\sigma} - \tilde{n}_{-\sigma}) \\ &\quad + [(\mu_\sigma \mu'_\sigma|\tilde{w}|\mu_\sigma \mu'_\sigma) - (\mu_\sigma \mu'_\sigma|\tilde{w}|\mu'_\sigma \mu_\sigma)] \\ &\quad \times (\tilde{n}_{\mu\sigma} - \tilde{n}_\sigma)(\tilde{n}_{\mu'\sigma} - \tilde{n}_\sigma)\} \\ &= \frac{1}{2} \sum_{\boldsymbol{R}\sigma\mu\mu'} \{(\mu_\sigma \mu'_{-\sigma}|\tilde{w}|\mu_\sigma \mu'_{-\sigma})\tilde{n}_{\mu\sigma}\tilde{n}_{\mu'-\sigma} \\ &\quad + [(\mu_\sigma \mu'_\sigma|\tilde{w}|\mu_\sigma \mu'_\sigma) - (\mu_\sigma \mu'_\sigma|\tilde{w}|\mu'_\sigma \mu_\sigma)]\tilde{n}_{\mu\sigma}\tilde{n}_{\mu\sigma}\} \\ &\quad - \frac{1}{2} \sum_{\boldsymbol{R}\sigma} \{U(N - \tilde{n}_\sigma) - J(N_\sigma - \tilde{n}_\sigma)\}N_\sigma, \quad (23) \end{aligned}$$

$$N_\sigma = \sum_\mu \tilde{n}_{\mu\sigma} = (2l+1)\tilde{n}_\sigma.$$

In the second equality, use of the sum rules ((13), (14)) is made. N is the number of electrons occupying a whole correlated l-shell, N_σ is that for one spin sort. There is no danger of confusing it with the total electron number in Eqs. (1)–(5), the latter does not appear any more in the sequel.

The corresponding U-potential is, again most easily with use of the sum rules,

$$\begin{aligned} \frac{\partial e^{U,\mathrm{AMF}}}{\partial \tilde{n}_{\mu\sigma}} &= \sum_{\mu'} \{(\mu_\sigma \mu'_{-\sigma}|\tilde{w}|\mu_\sigma \mu'_{-\sigma})(\tilde{n}_{\mu'-\sigma} - \tilde{n}_{-\sigma}) \\ &\quad + [(\mu_\sigma \mu'_\sigma|\tilde{w}|\mu_\sigma \mu'_\sigma) - (\mu_\sigma \mu'_\sigma|\tilde{w}|\mu'_\sigma \mu_\sigma)] \\ &\quad \times (\tilde{n}_{\mu'\sigma} - \tilde{n}_\sigma)\}. \quad (24) \end{aligned}$$

One weak point of this version is that it yields no contribution at all in case of orbital-independent occupation numbers $\tilde{n}_{\mu'\sigma} = \tilde{n}_\sigma$. This is, for instance, the case of a half-filled completely spin polarized shell (e.g. 4f-shell of Gd). In the Gd case this is at least not too bad, as the LSDA gives nearly the right spin polarization energy of Gd, although there is a problem with the right magnetic ground state (obtained anti-ferromagnetic in LSDA).

2.4. The 'atomic limit' LSDA + U functional

With the Gd case in mind and aiming at a better description of the photoelectron spectra, Czyżyk and Sawatzky introduced another functional in [13] which they labeled 'atomic limit' (AL). At least regarding its relation to photoemission it should rather be considered a model for the quasiparticle self-energy Σ instead

of being related to e^U. Nevertheless, it was given in an e^U-form as (again $l(n_{ss'}(\boldsymbol{r}),\dots)=l_{\mathrm{LSDA}}$)

$$\begin{aligned} e^{U,\mathrm{AL}} =& \frac{1}{2}\sum_{\boldsymbol{R}\sigma\mu\mu'}\{(\mu_\sigma\mu'_{-\sigma}|\tilde{w}|\mu_\sigma\mu'_{-\sigma})\tilde{n}_{\mu\sigma}\tilde{n}_{\mu'-\sigma} \\ &+ [(\mu_\sigma\mu'_\sigma|\tilde{w}|\mu_\sigma\mu'_\sigma)-(\mu_\sigma\mu'_\sigma|\tilde{w}|\mu'_\sigma\mu_\sigma)]\tilde{n}_{\mu\sigma}\tilde{n}_{\mu\sigma}\} \\ &- \frac{1}{2}\sum_{\boldsymbol{R}}\left\{UN(N-1)-J\sum_\sigma N_\sigma(N_\sigma-1)\right\} \\ =& e^{U,\mathrm{AMF}}+\frac{1}{2}\sum_{\boldsymbol{R}\sigma}(U-J)(1-\tilde{n}_\sigma)N_\sigma. \end{aligned} \tag{25}$$

The corresponding U-potential is

$$\frac{\partial e^{U,\mathrm{AL}}}{\partial\tilde{n}_{\mu\sigma}}=\frac{\partial e^{U,\mathrm{AMF}}}{\partial\tilde{n}_{\mu\sigma}}-(U-J)\left(\tilde{n}_\sigma-\frac{1}{2}\right). \tag{26}$$

One characteristic feature of this U-potential is that in case of an isolated shell it moves the occupied states downward by $(U-J)/2$ and the unoccupied states upward by $(U-J)/2$ independent of the shell occupation. By way of contrast, the center of the AMF spin subshell potential split moves up with increasing subshell occupation (so that the shift of the occupied levels is zero in the case of a filled spin subshell and likewise the shift of the unoccupied levels of an empty spin subshell; this way yielding no shift at all in Gd). On the other hand, the AL $4f$-level splitting of Gd is approximately doubled compared to LSDA which is a rather good result in the sense of a self-energy correction.

2.5. The Kohn–Sham Hamiltonian matrix element and the total energy

Here the formulas are presented, which actually are implemented. For the sake of simplicity, the correlated orbitals are identified with selected local basis orbitals as discussed at the beginning of Section 2.2. The diagonalization of the occupation matrix, although greatly simplifying the analytical derivations, does not have advantages when coded, since the diagonalizing transformation is site and spin dependent. Therefore, the full occupation matrix $\tilde{n}_{mm'\sigma}$ is kept. (In the following, the site index of all quantities is dropped. If multiple sites with correlated states are needed, the formulas apply to all sites separately.) The matrix is obtained from the KS states:

$$\tilde{n}_{mm'\sigma}=\sum_{n\boldsymbol{k}}c^{n\boldsymbol{k}}_{m\sigma}n_{n\boldsymbol{k}\sigma}c^{n\boldsymbol{k}*}_{m'\sigma}. \tag{27}$$

Integration is over the irreducible part of the Brillouin zone and a symmetrization projector is applied afterwards to get the result for the full zone.

The AMF U-potential matrix as given in the text after Eq. (8) becomes

$$\begin{aligned} v^{\mathrm{AMF}}_{m'm\sigma} =& \sum_{\sigma'}\sum_{\mu\mu'}(\tilde{n}_{\mu\mu'\sigma'}-\tilde{n}_{\sigma'}\delta_{\mu\mu'}) \\ &\times[(m'\mu'|\tilde{w}|m\mu)-\delta_{\sigma\sigma'}(m'\mu'|\tilde{w}|\mu m)] \end{aligned} \tag{28}$$

with the property $\mathrm{Tr}\, v^{\mathrm{AMF}}_{mm'\sigma}\equiv 0$ for each σ separately. (Tr means the trace of the (m,m')-matrix; it vanishes due to the sum rules (13), (14).) There is no such property of the AL potential since here the up and down shifts are independent of the shell occupation. The interaction matrix elements are taken to be spin independent. They are calculated from the Slater parameters according to Eq. (16). (Recall that the $\tilde{F}_i$ are external parameters, not variational.)

The projection part of Eq. (8) gives only Kronecker deltas. Thus the matrix elements of the KS equation are modified by $v^{\mathrm{AMF}}_{mm'\sigma}$ for every block of correlated orbitals. The eigenvalue sum over the occupied bands yields the band structure energy E^{B}. The kinetic energy is obtained from it by subtracting the expectation values of all potentials entering the KS equation. Besides the LSDA like expressions a term

$$V^{\mathrm{AMF}}=\sum_{mm'\sigma}v^{\mathrm{AMF}}_{m'm\sigma}\tilde{n}_{mm'\sigma} \tag{29}$$

is to be subtracted. Here, capitals E, V denote total energy contributions corresponding to the solution of the KS equations. E without superscript is the l.h.s. of Eq. (5). Since the AMF-potential matrix is traceless, a constant diagonal term may be added to the occupation matrix to obtain from (28) and (23)

$$V^{\mathrm{AMF}}=\sum_{mm'\sigma}v^{\mathrm{AMF}}_{m'm\sigma}(\tilde{n}_{mm'\sigma}-\tilde{n}_\sigma\delta_{mm'})=2E^{U,\mathrm{AMF}}. \tag{30}$$

($E^{U,\mathrm{AMF}}$ is the value of (23) for the occupation matrix corresponding to the KS solution.) Finally, the LSDA + U, kinetic and total energy are

$$T=E^{\mathrm{B}}-V^{\mathrm{LSDA}}-2E^{U,\mathrm{AMF}}, \tag{31}$$

$$E=E^{\mathrm{LSDA}}-E^{U,\mathrm{AMF}}, \tag{32}$$

where V^{LSDA} and E^{LSDA} (the latter expressed through E^{B}) mean the formula expressions of the LSDA calculated with the LSDA + U KS orbitals and (in the case of E^{B}) with the LSDA + U KS band energies.

The U^{AL}-potential matrix may be written as

$$\begin{aligned} v^{\mathrm{AMF}}_{m'm\sigma} =& \sum_{\sigma'}\sum_{\mu\mu'}\tilde{n}_{\mu\mu'\sigma'}[(m'\mu'|\tilde{w}|m\mu)-\delta_{\sigma\sigma'}(m'\mu'|\tilde{w}|\mu m)] \\ &- v^{\mathrm{dc}}_\sigma\delta_{mm'} \end{aligned} \tag{33}$$

with

$$v^{\mathrm{dc}}_\sigma=U(N-\frac{1}{2})-J(N_\sigma-\frac{1}{2}). \tag{34}$$

Again, every block belonging to a correlated orbital in the Hamilton matrix is modified by adding $v^{\mathrm{AL}}_{mm'\sigma}$.

A somewhat more involved algebra yields

$$V^{\mathrm{AL}} \equiv \sum_{mm'\sigma} v^{\mathrm{AL}}_{m'm\sigma}\tilde{n}_{mm'\sigma} = 2E^{U,\mathrm{AL}} - \frac{U-J}{2}N. \tag{35}$$

Thus, the final result is

$$T = E^{\mathrm{B}} - V^{\mathrm{LSDA}} - 2E^{U,\mathrm{AL}} + \frac{U-J}{2}N, \tag{36}$$

$$E = E^{\mathrm{LSDA}} - E^{U,\mathrm{AL}} + \frac{U-J}{2}N. \tag{37}$$

3. Applications to cuprates

The structure of the 2D cuprates considered here may be described by the formula $B(CuO_2)_nCa_{n-1}$, where B denotes the block layer which separates stacks of n CuO_2-planes with Ca planes sandwiched in between.

The LSDA + U approach was applied to three compounds ($CaCuO_2$ $(n=\infty)$, $Sr_2CuO_2Cl_2$ $(n=1)$ and $Bi_2Sr_2CaCu_2O_8$ $(n=2)$) with the focus on the orbital analysis of relevant bands. While the band structure gap between occupied and unoccupied bands is a ground state property (jump of the chemical potential as function of the particle number at zero temperature), the whole band structure refers to the excitation spectrum, and the KS band structure need not compare to photoemission, say. Nevertheless, although there is no deeper reason that the best LSDA + U potential for the KS equations should be close to the electron self-energy, there is some hope that like for weakly correlated systems the LSDA + U band structure could again provide also an approximation to the quasi-particle spectrum. One should, however, be aware that in principle the best KS U-value need not be the same as the best U-value in Hubbard-type model Hamiltonians. The latter value should for instance be used in dynamical mean-field theory which is an approach to the electron Green's function (self-energy). A satisfactory link of the U-value to the KS variational quantities, the KS orbitals and KS orbital occupation numbers, is still missing. For LSDA + U as a Hohenberg–Kohn model the most relevant results are ground state properties as structural parameters (lattice constants, Wyckoff parameters), magnetic structure and magnetic polarization energy and band gap. The lattice parameters for the cuprates are obtained in the usual ± 2 p.c. agreement with experiment. They will not be considered in the following.

The FPLO version used is 3.00–5 [18]. Here, the program settings are summarized, which are unique to all calculations. The LSDA version is that of Perdew and Zunger [19]. The Cu 3d orbitals are taken to be the correlated orbitals. For the sake of comparison, the same Slater parameters were used for all calculations: $U = 8.16$ eV (0.3 hartree), $J = 1$ eV ($F_2 = 9$ eV, $F_4 = 5$ eV). The orbitals were optimized in the non-magnetic structures and the resulting compression radii were used also for the antiferromagnetic (AFM) LSDA-U calculations. Unless explicitly else stated the "around mean field" (AMF) functional is used.

3.1. $CaCuO_2$

The 'infinite layer' cuprate $CaCuO_2$ (no block layer B) does not exist in nature, but there is an isostructural compound $Ca_{0.85}Sr_{0.15}CuO_2$. It is considered here first because the bands of this infinite cuprate stack are not perturbed by hybridization with block layer states and hence in this sense are pure. The experimental lattice parameters of $Ca_{0.85}Sr_{0.15}CuO_2$ [20] are taken for the fictitious $CaCuO_2$. The antiferromagnetic unit cell is shown in Fig. 1. The space group is $I4/mmm$ (139). The distance along Cu–O–Cu is $d_a = 3.86$ Å and the distance in z-direction between adjacent CuO_2 layers is $d_c = 3.20$ Å. (For all compounds considered here d_a is the lattice constant of the non-magnetic cuprate plane, while d_c is the distance in z-direction between adjacent cuprate multilayers $[(CuO_2)_nCa_{n-1}]$. For $CaCuO_2$ it is the CuO_2 plane distance. It also gives the periodicity of the multilayers in z-direction, ignoring a centering shift perpendicular to the z-direction.)

The AFM lattice constants are $a_0 = b_0 = \sqrt{2}d_a$, $c_0 = 2d_c$. The atom positions are Ca $(0,\frac{1}{2},\frac{1}{4})$, Cu $(0,0,0)$, Cu $(0,0,\frac{1}{2})$ and O $(\frac{1}{4},\frac{1}{4},0)$. Table 1 gives the FPLO basis set.

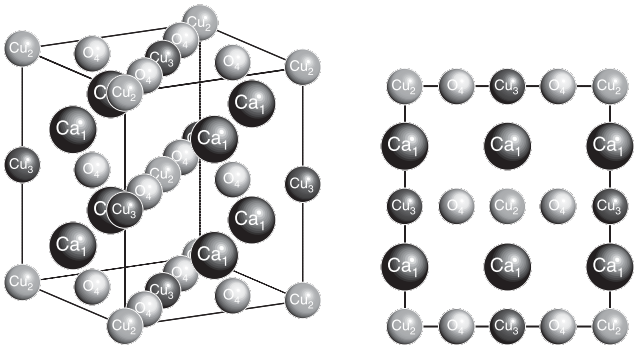

Fig. 1. Unit cell of antiferromagnetic $CaCuO_2$; Cu_2 spin up, Cu_3 spin down.

Table 1
Basis set for $CaCuO_2$

Atom	Core	Valence
Ca	1s 2s 2p	3s(−1) 3p(−1) 4s(1.1240) 4p(1.0927) 3d(−1)
Cu	1s 2s 2p	3s(−1) 3p(−1) 4s(1.3148) 4p(1.2648) 3d(1.3500)
O	1s	2s(1.2869) 2p(1.2822) 3d(−1)

Compression parameter for valence orbitals in parentheses.

The number of Fourier components was 1024 per atom and the k-mesh subdivision was $(6,6,6)$. Non-relativistic calculations were performed.

The symmetry points of the band structures presented below refer to the Brillouin zone of the antiferromagnetic cuprate plane (a square of edge length $2\pi/(\sqrt{2}d_a)$). For better comparison to the literature we relate it to the non-magnetic Brillouin zone which is a rotated by 45° square of edge length $2\pi/d_a$. In units of π/d_a we have $\Gamma,(Z)=(0,0,\zeta)$, $X,(R)=(\frac{1}{2},\frac{1}{2},\zeta)$ and $M,(A)=(1,0,\zeta)$. The first labels refer to $\zeta=0$ and the labels in parentheses refer to $\zeta=1\doteq\pi/d_c$. ((0,0,1) is the Z point of a simple tetragonal cell of lattice constant $c=d_c$.)

Calculations within LSDA and LSDA + U were performed. As usual for the cuprates, the LSDA gives a metallic ground state. The KS band structure is shown in Fig. 3. The spaghetti below the Fermi level (here and in all following figures put equal to zero) consists of hybridized Cu-3d and O-2p states, with the bonding combinations at the bottom and the antibonding bands formed of the orbitals of Fig. 2 crossing the Fermi level. Non-bonding combinations are in between. The unoccupied bands above the Fermi level start with Cu-4s and Cu-4p character and then enter a bunch of Ca-3d bands above 5 eV.

The same bands weighted (by linewidth) with the square of the coefficient of selected basis orbitals in the KS state are shown in Fig. 4. Bands not seen on these panels have a negligible contribution from the corresponding orbital. From the upper two panels one can read off a $(\mathrm{Cu-O})_\sigma$ covalency split of more than 5 eV while the third panel shows a (O–O) covalency split of about 3 eV. One further observes that the O_σ orbitals and the O_z orbitals hybridize also with the Cu 4s and 4p orbitals while the in-plane O_π orbitals hybridize additionally with the Ca 3d orbitals (not shown). Figs. 3 and 4 are presented here for comparison with the LSDA + U results shown below.

Experimentally, $(Ca_{0.85}Sr_{0.15})CuO_2$ is an AFM insulator with a band gap of more than 1 eV and a Néel temperature $T_N\approx 540$ K. The U-functional cures this deficiency and one finds an AFM solution with a spin polarization energy $\Delta E=27.9$ mhartree per formula unit below the Pauli-paramagnetic (PM) state. The site projected copper 3d moment is $0.71\mu_B$ and the total copper spin moment is $0.69\mu_B$ (reduced by negative 3s3p moments).

The already discussed two relevant molecular orbitals (MO) of Fig. 2 are the candidates for the highest occupied molecular orbital (HOMO) in the correlated electronic structure of cuprates, that is, those MOs which are relevant for the valence band edge. The LSDA + U KS bands of $CaCuO_2$ with the AMF and AL functionals are shown in Fig. 5. The main difference between both functionals is found in the unoccupied bands. As to be expected for a more than half-filled shell, the upper Hubbard band of (Cu-3$d_{x^2-y^2}$ and O-2p_σ character, see below) lies higher in the AMF case compared to AL. In AL this band is the lowest unoccupied band. In the occupied part near the Fermi level the differences are small, while far below larger differences are found due to the different position of the lower Hubbard band and thus to different hybridization. Since this paper focuses on the occupied bands near the Fermi level, the differences are not very relevant, and all further results are presented for the AMF functional.

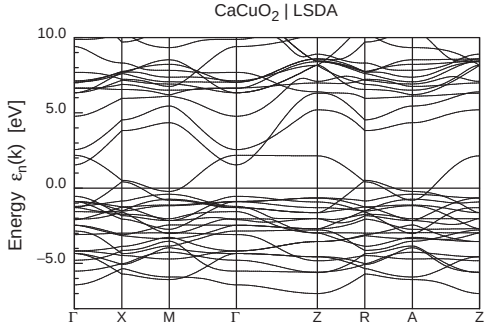

Fig. 3. LSDA band structure of $CaCuO_2$.

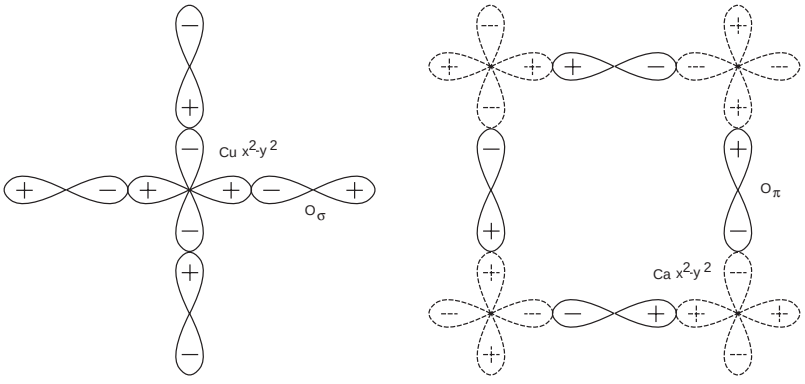

Fig. 2. Left: Antibonding ($\boldsymbol{k}=(\pi,\pi,0)$) $dp\sigma$-orbital commonly assumed as the HOMO that forms the Zhang–Rice singlet together with the nominal Cu-d hole [21,22]. Right: O–O antibonding ($\boldsymbol{k}=0$) in-plane $p\pi$-orbital, lifted up by crystal field and weakly hybridized with Ca-d orbitals in adjacent layers: the true HOMO of the LSDA + U model [23,24].

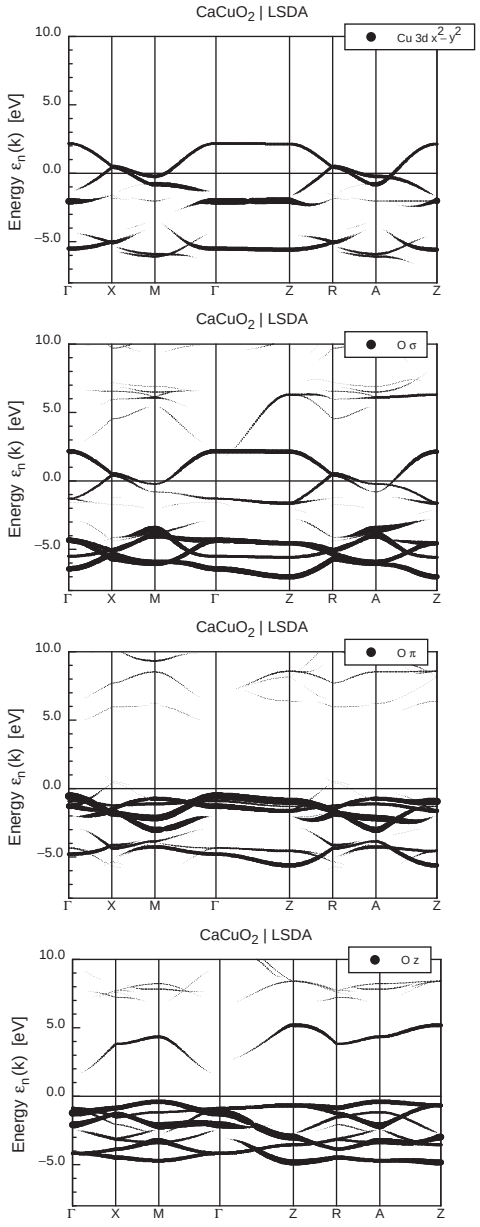

Fig. 4. LSDA result for $CaCuO_2$. From top: orbital weight of the Cu-$3d_{x^2-y^2}$ orbital, the O-$2p_\sigma$ orbitals, the O-$2p_\pi$ and the O-$2p_z$ orbitals.

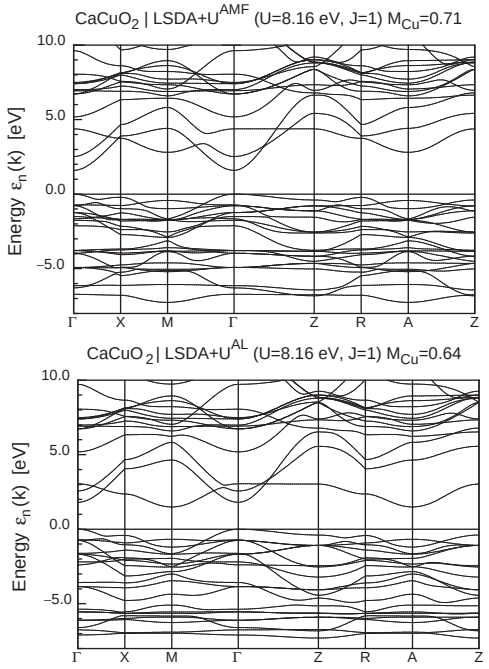

Fig. 5. LSDA + U band structure of $CaCuO_2$. Top: AMF, bottom: AL.

Recall that all density functionals in practical use are model functionals. Hence, with respect to the physical relevance of the presented results, two independent issues are to be addressed. The first is, given a model functional like LSDA, or LSDA + U in the AMF or AL variants, what is the numerical accuracy of the solution for the corresponding KS bands and for the total energy of that model. This has been carefully analyzed to be in the ten meV range for the occupied bands and better than a tenth of an eV for the lowest unoccupied bands. (The error due to basis incompleteness increases with increasing band energy.) This numerical accuracy is by far sufficient for addressing the second issue: How does the model compare to quantum mechanics, that is, to experiment. Here, the answer is a phenomenological one, in the present case saying that the LSDA + U does much better than the LSDA both with respect to the excitation gap and to the polarization of the ground state. Hence, other details of the LSDA + U results can also be considered with more confidence than the corresponding LSDA results.

In Fig. 6 the orbital weights to the AMF bands in analogy to Fig. 4 is shown. First, it is clearly seen that the upper and lower Hubbard band is formed by Cu-$3d_{x^2-y^2}$ and O-$2p_\sigma$ orbitals. At the valence band edge (points X and R shown, but without noticeable dispersion on the whole line X–R in z-direction of the $\boldsymbol{k}$-space) O-$2p_\sigma$ and O-$2p_\pi$ contribute equally strongly while the Cu-$3d_{x^2-y^2}$ orbital contribution is largely suppressed compared to the LSDA result. This suppression of the Cu contribution to valence holes in cuprates is confirmed by experiment [25]. The O-$2p_\pi$ contribution on the other hand is strongly enhanced compared to LSDA, a new result which is missed in most model Hamiltonian treatments in the literature where the O-$2p_\pi$ degree of freedom is excluded from the Hamiltonian in most cases. Other orbitals do not contribute. Hence, on the line X–R the highest occupied band is mainly a hybrid of O-$2p_\sigma$ and O-$2p_\pi$. These band states are assumed to form the Zhang–Rice singlet with the nominal $3d$-hole on the Cu site (upper Hubbard state) [22]. The bandwidth of the highest valence band is about 1 eV due to hybridization with a flat band 1 eV below the Fermi level. On the line X–M (R–A) the O-$2p_\sigma$

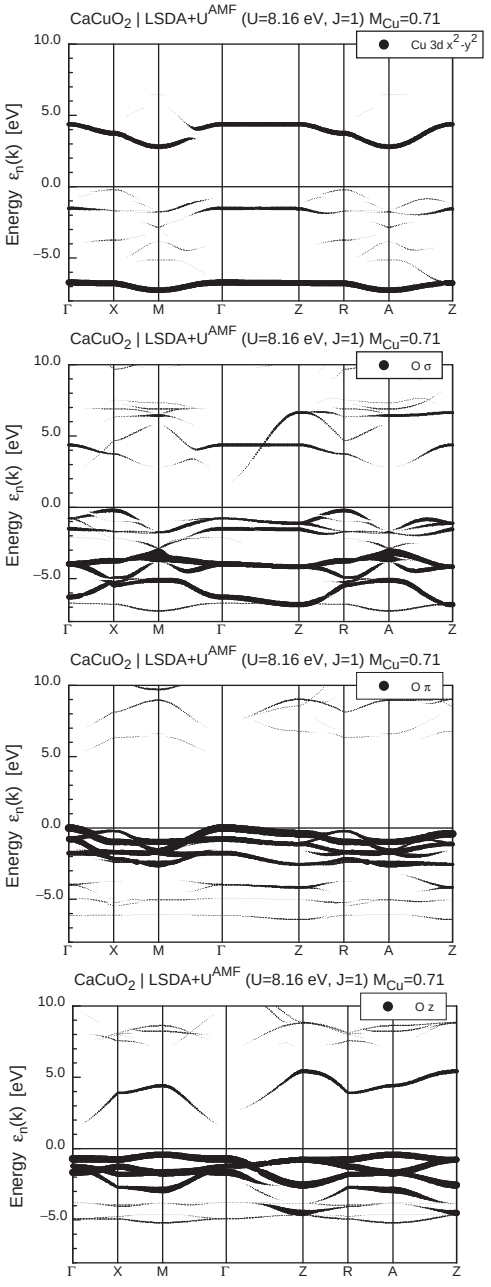

Fig. 6. From top to bottom: orbital weight of the Cu-3$d_{x^2-y^2}$ orbital, the O-2p_σ orbitals, the O-2p_π and the O-2p_z orbitals.

contribution fades away towards M (A) due to this hybridization. In LSDA the O-2p_π orbitals do practically not contribute to this band which led to the neglect of that orbital in model Hamiltonians. This failure of the LSDA is mainly due to the fact that in LSDA the O-2p_π bands are deeper in energy compared to the Cu-3$d_{x^2-y^2}$–O-2p_σ bands.

The absolutely highest occupied band in the LSDA + U result is a pure O-2p_π band (at Γ) which therefore is in energetic competition with the Zhang–Rice state when adding additional holes. The O-2p_π bands show a considerable dispersion in z-direction which comes from a weak hybridization with the unoccupied Ca-3$d_{x^2-y^2}$ orbitals. The Cu 4s orbitals do not contribute at the valence band edge. They are mixed into the unoccupied states and are also slightly mixed into O-2p_σ states about 1.5 eV below the Fermi level on the line M–A.

3.2. $Sr_2CuO_2Cl_2$

The single-layer compound $Sr_2CuO_2Cl_2$ is probably the most two-dimensional of all cuprates. The block layer consists of 2 SrCl layers which separate single CuO_2 planes. Between these SrCl layers crystals are easily cleaved, whence most photoemission data on undoped planar cuprates are recorded from this material. Two adjacent cuprate planes are shifted horizontally by a shift vector $(\frac{1}{2},\frac{1}{2},0)$ relative to each other, which produces a body centered non-magnetic unit cell. The large distance of cuprate planes from each other prevents valence state coupling in z-direction. The AFM cell has base centered orthorhombic symmetry and is shown in Fig. 7.

The standard cell choice for the orthorhombic cell, which has also to be used in the FPLO code results in c-base centering. (The stacking direction is the b-direction and the cuprate plane is the c,a plane.) The space group is $Cmmm$ (65). The cell parameters are $d_a = 3.973$ Å and $2d_c = 15.618$ Å [26]. The lattice constants of the AFM cell are $a_0 = c_0 = \sqrt{2}d_a$, $b_0 = 2d_c$. The atom positions are Cu $(0,\frac{1}{2},\frac{1}{2})$, Cu $(0,0,0)$, O $(-\frac{1}{4},0,-\frac{1}{4})$, Cl $(0,-0.317,\frac{1}{2})$, Cl $(0,0.183,0)$, Sr $(0,-0.107,\frac{1}{2})$ and Sr $(0,0.393,0)$. Table 2 gives the basis set. The number of

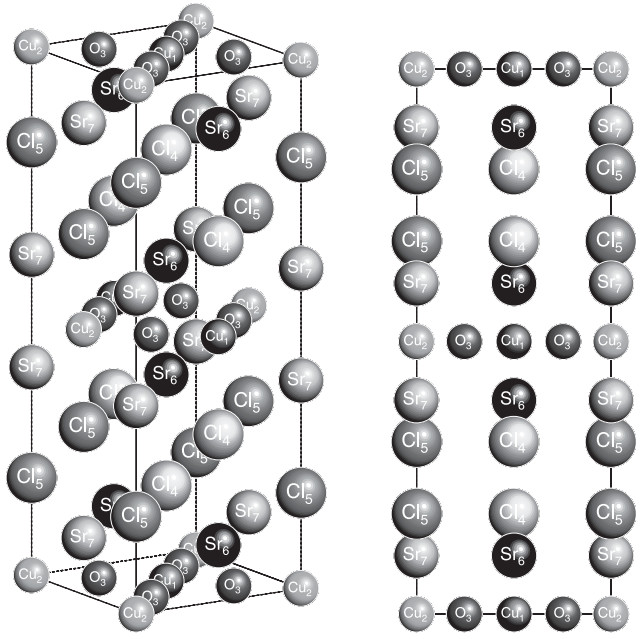

Fig. 7. Unit cell of antiferromagnetic $Sr_2CuO_2Cl_2$; Cu_1 spin up, Cu_2 spin down.

Table 2
Basis set for $Sr_2CuO_2Cl_2$

Atom	Core	Valence
Cu	1*s* 2*s* 2*p*	3*s*(−1) 3*p*(−1) 4*s*(1.2300) 4*p*(1.1199) 3*d*(1.3148)
O	1*s*	2*s*(1.2580) 2*p*(1.2377) 3*d*(1.1162)
Cl	1*s* 2*s* 2*p*	3*s*(1.1518) 3*p*(1.1338) 3*d*(1.0852)
Sr	1*s* 2*s* 2*p* 3*s* 3*p* 3*d*	4*s*(−1) 4*p*(−1) 5*s*(1.1360) 5*p*(1.0816) 4*d*(1.1503)

Compression parameter for valence orbitals in parentheses.

Fourier components was 1000 per atom and the k-mesh subdivision was $(12, 12, 12)$. Scalar relativistic calculations are performed. For the sake of comparison the stacking direction is further on denoted z and the cuprate plane as the x, y-plane. The symmetry points are chosen corresponding to the scheme described in the previous subsection.

The site projected copper 3*d* moment of the LSDA + U result is $0.758\mu_B$ and the total copper spin moment is $0.748\mu_B$. In Fig. 8 the orbital weights for the relevant bands are shown. The situation is rather similar to that of $CaCuO_2$, so only the differences are pointed out.

The "Zhang–Rice" band is slightly higher and touches the valence band edge at X and R. The intersecting band is correspondingly lower at the line M–A, as a consequence the width of the upper valence band is about 1.5 eV and the fading of the O-2p_σ character on the lines X–M and R–A is less pronounced, a reduction of about 50 p.c. remains. The z-dispersion of the O-2p_π band on the line Γ-Z has gone as there are no Ca-3*d* states present for hybridization. There is a marked 2D character of the compound.

The quasiparticle low-energy dispersion measured by ARPES (single hole excitation) is shown in Fig. 9. A detailed discussion is found in [27,28]. The left part of the experimental spectra (from (0,0) to $(\frac{\pi}{2}, \frac{\pi}{2})$) compares nicely with the O-2p_σ dominated LSDA + U band on the line $\Gamma - X$ (second panel of Fig. 8) and the right part (from $(\frac{\pi}{2}, \frac{\pi}{2})$ to $(0, \pi)$) with the same LSDA + U band on the line X–M. Even the reported fading ARPES intensity when going from X towards M (see also [29]) agrees with the fading O-2p_σ projection of that band. Nevertheless, the experimental band width is smaller by a factor of about two to three and the situation on the line $\Gamma - M$ is less clear although the comparison of only the O-2p_σ projected bands (second panel of Fig. 8, cf. the discussion of models above) to model results contained in Fig. 9 is not so bad. After all, LSDA + U accounts for electron correlations still rather grossly.

3.3. $Bi_2Sr_2CaCu_2O_8$

The bilayer compound $Bi_2Sr_2CaCu_2O_8$ has a double layer of cuprate planes separated by block layers. The

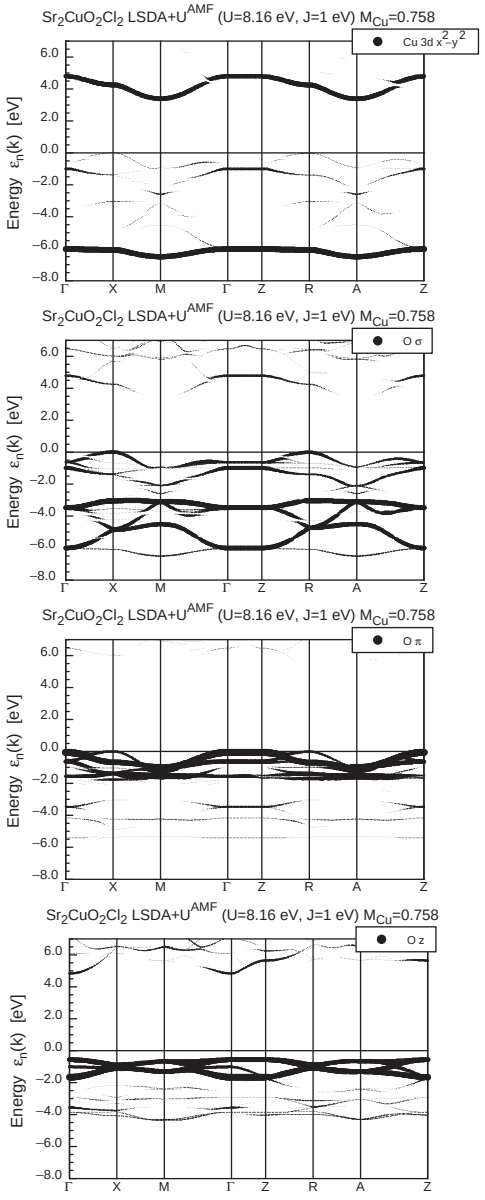

Fig. 8. Same as Fig. 6 for $Sr_2CuO_2Cl_2$.

block layer consists of two $BiSrO_2$ layers between which crystals cleave equally easily as in the previous case and also favor the material for photoemission. Adjacent double layers are again shifted horizontally by a shift vector $(\frac{1}{2}, \frac{1}{2}, 0)$ relative to each other, which produces a body centered tetragonal non-magnetic cell. The hypothetic AFM cell again is assumed base centered orthorhombic.

The cell parameters are again given in the c-base centered setting, resulting in the b-axis being the stacking direction. The space group is *Cmmm* (65). The cell parameters are $d_a = 3.817$ Å and $2d_c = 30.6$ Å. The lattice constants of the AFM cell are $a_0 = c_0 = \sqrt{2}d_a$, $b_0 = 2d_c$. The atom positions are Ca $(0, \frac{1}{4}, \frac{1}{4})$, Sr $(0, 0.3597, \frac{1}{4})$, Sr $(0, 0.1403, \frac{1}{4})$, Bi $(0, -0.4478, \frac{1}{4})$, Bi

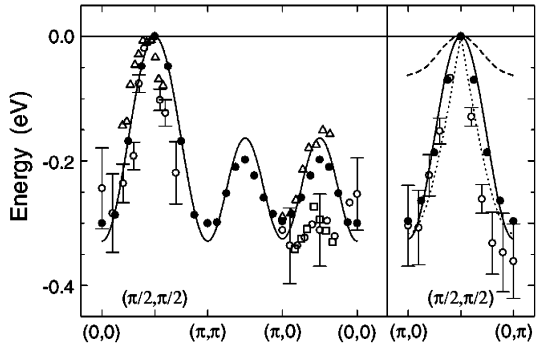

Fig. 9. Energy dispersion of quasiparticles for $Sr_2CuO_2Cl_2$ [27]. The energy zero is put at the top of the band, about 0.7 eV below Fermi level. Open symbols: experimental data; solid circles: self-consistent Born approximation for a t–t'–t''–J model; solid line: tight-binding fit; dashed: t–J model; dotted: spinon model dispersion.

Table 3
Basis set for $Bi_2Sr_2CaCu_2O_8$

Atom	Core	Valence
Ca	1*s* 2*s* 2*p*	3*s*(−1) 3*p*(−1) 4*s*(1.1298) 4*p*(1.1210) 3*d*(1.2286)
Sr	1*s* 2*s* 2*p* 3*s* 3*p* 3*d*	4*s*(−1) 4*p*(−1) 5*s*(1.1239) 5*p*(1.0717) 4*d*(1.1435)
Bi	1*s* 2*s* 2*p* 3*s* 3*p* 3*d* 4*s* 4*p* 4*d* 4*f*	5*s*(−1) 5*p*(−1) 6*s*(1.3570) 6*p*(1.2922) 5*d*(1.4752)
Cu	1*s* 2*s* 2*p*	3*s*(−1) 3*p*(−1) 4*s*(1.2229) 4*p*(1.1549) 3*d*(1.3060)
O_1	1*s*	2*s*(1.2464) 2*p*(1.2177) 3*d*(−1)
O_2	1*s*	2*s*(1.1766) 2*p*(1.1895) 3*d*(−1)
O_3	1*s*	2*s*(1.0683) 2*p*(1.0951) 3*d*(−1)

Compression parameter for valence orbitals in parentheses.

$(0,-0.0522,\frac{1}{4})$, Cu $(0,-0.3040,\frac{1}{4})$, Cu $(0,-0.1960,\frac{1}{4})$, O_1 $(-\frac{1}{4},0.1960,0)$, O_2 $(0,-0.1250,\frac{1}{4})$, O_2 $(0,-0.3750,\frac{1}{4})$, O_3 $(0,0.0450,\frac{1}{4})$ and O_3 $(0,0.4550,\frac{1}{4})$. The two Sr, Bi, O_2, O_3 and Cu atoms are equivalent in the non-magnetic cell. The O_1 atom is that of the cuprate plane. The two Cu spins are antiferromagnetically ordered in the AFM cell. Table 3 gives the basis set. The number of Fourier components was 500 per atom and the k-mesh subdivision was $(8,8,8)$. Again, scalar relativistic calculations were performed and the symmetry points in $\boldsymbol{k}$-space are chosen corresponding to the scheme described in Section 3.2.

For this material both the LSDA and LSDA + U yield a metallic ground state with Cu–O bands and Bi bands crossing the Fermi level. While the LSDA results in a non-magnetic solution, the LSDA + U calculation yields a stable AFM state. The site projected copper 3d moment is $0.696\mu_B$ and the total copper spin moment is $0.684\mu_B$.

Fig. 10 shows both the LSDA and LSDA + U bands of $Bi_2Sr_2CaCu_2O_8$ close to the Fermi level. For a better orientation in the band character the Cu-3$d_{x^2-y^2}$ projected bands are also shown. Note that the LSDA + U results on the right panels have twice as many bands as the LSDA results on the left panels due to the AFM order of the former ground state. The bands crossing the Fermi level and not seen in the lower panels are Bi bands (more precisely BiO bands hybridized with orbitals of the block layer oxygen).

The splitting of the Cu-3$d_{x^2-y^2}$ projected LSDA bands crossing the Fermi level on the line X–M (R–A) is the much discussed bilayer splitting between bonding and antibonding combinations of the CuO states in both CuO_2 layers of the bilayer [28]. The coupling of those states is mainly due to a small hybridization with Cu-4s states, and this part of the coupling has $k_x^2 - k_y^2$ symmetry. Hence, the splitting is maximum ($\sim$0.25 eV) at point M (A) and nearly zero at point X (R) although a very small splitting remains there due to a small direct coupling. It is readily seen by a simple symmetry argument that in the AFM state this splitting must be zero on the whole line X–M (R–A), if spin-orbit coupling is neglected. Accordingly all bands on the right panels of Fig. 10 are twofold degenerate on these lines and do not show a bilayer splitting there. This only develops away from these lines, for instance in the X-Γ and M-Γ directions. However, the Cu-3$d_{x^2-y^2}$ projected LSDA + U bands on the right lower panel show around M and A another splitting of approximately the same magnitude which is due to the crossing of another oxygen band. This point has never been considered in the literature to date.

Note also that the non-magnetic structure of the left panels has a larger Brillouin zone so that the rising band from Γ to X continues to rise from $X = (\frac{1}{2},\frac{1}{2},0)$ to the Brillouin zone corner (1,1,0), whereas the AFM structure of the right panels has a charge transfer gap (dominated by U and hence much larger than the exchange splitting) at X, which now lies on the Brillouin zone boundary, and the conduction band has its maximum at X. On the other hand, the band pair close to the Fermi level on the line $\Gamma - Z$ on the upper right panel is on the line $(1,1,\zeta)$ in the non-magnetic state and not shown on the upper left panel. To illustrate the charge transfer gap, the LSDA + U band structure projected on Cu-3$d_{x^2-y^2}$ is shown once more in Fig. 11 for a larger energy window.

Experimentally, the oxygen in the block layers of $Bi_2Sr_2CaCuO_8$ is volatile and its stoichiometry is governed by thermodynamics. Moreover, the geometry of the block layer is distorted in a disordered way compared to the ideal structure used in the calculation. In the recent, highest resolution photoemission spectra [28], Fermi surface pockets around point M which should be present due to the Bi bands in both the LSDA and LSDA + U results are not seen. Hence, one could assume that they are pushed away from the Fermi level (together with the oxygen bands on Γ-Z) by a distortion

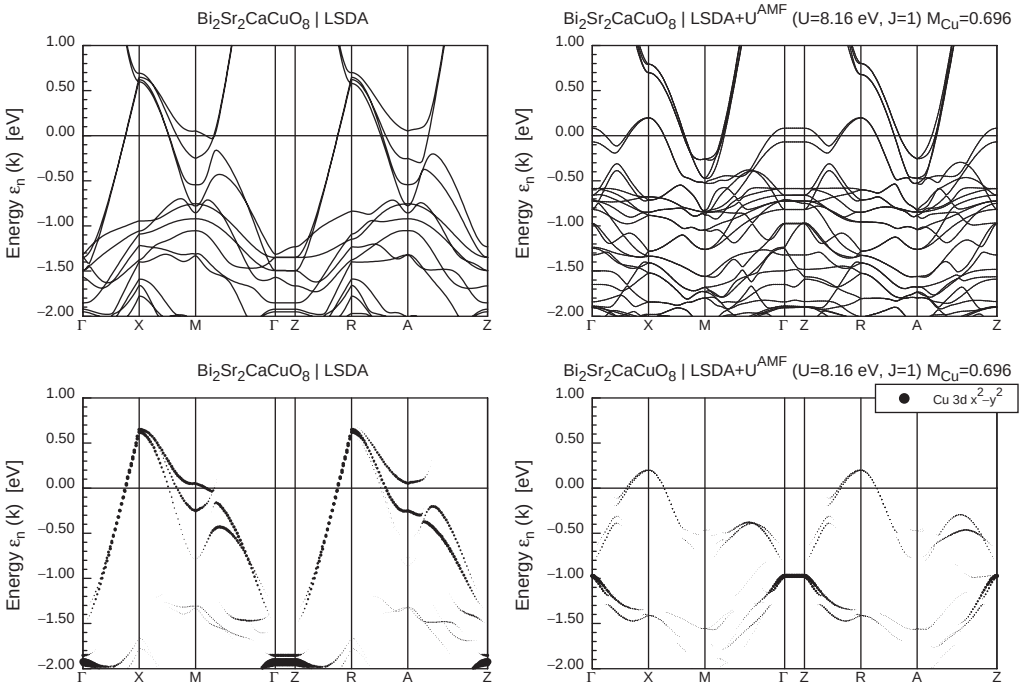

Fig. 10. $Bi_2Sr_2CaCu_2O_8$: left: LSDA band structure and Cu-3$d_{x^2-y^2}$ orbital weights, right: LSDA + U^{AMF} band structure and weights.

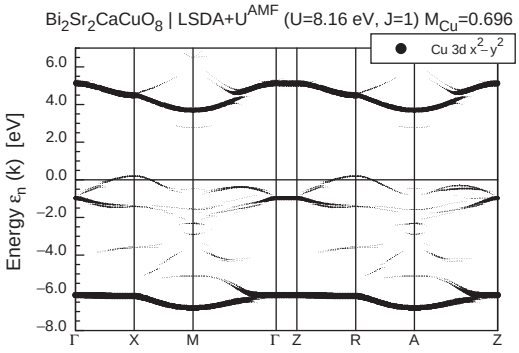

Fig. 11. $Bi_2Sr_2CaCu_2O_8$: LSDA + U^{AMF} Cu-3$d_{x^2-y^2}$ orbital weights.

potential. Correspondingly, the Fermi level would be lowered to ensure the electron count. This would be a big problem for the LSDA band structure where not only the antibonding bilayer split band would have an electron Fermi surface closed around Γ but also the bonding one, both in contradiction to what is seen in photoemission. The LSDA + U band structure (lower right panel of Fig. 10) on the contrary would be in rather good agreement with photoemission if one wipes out the down folded bands of the AFM order which is not found in experiment. (The material cannot be reduced down to undoped CuO_2^{2-} planes.)

There would be another stark difference to what is discussed in the literature with respect to the bilayer splitting: If the band splitting around M and observed in photoemission would be a bilayer splitting, one should expect it to be strongly reduced when reducing the doping level to an underdoped superconductor which is regarded to develop strong AFM correlations (also seen in neutron scattering). It should be reduced to zero where AFM order sets in. The splitting of the LSDA + U bands of different origin on the contrary is to be expected largely independent of antiferromagnetic order and hence on doping.

3.4. Implications on magnetic interactions

Magnetic couplings may grossly be obtained from total energy differences of LSDA + U results for ferromagnetic and antiferromagnetic order; in more detail they may be obtained from calculated energies of spin spiral states [30].

For a more detailed understanding of their physics, a tight-binding model of the kind of Emery's model should be extracted from the LSDA + U results, which then may be down-mapped to a kind of a t–J model. For a hypothetic ferromagnetic order (assumed for the sake of simplicity) such a tight-binding model was derived in Ref. [24].

One main conclusion from the present orbital analysis is that in a large part of the Brillouin zone there is a strong hybridization of O-2p_σ with O-2p_π orbitals in bands hybridized with the Cu-3$d_{x^2-y^2}$ orbital. Furthermore, the O-2p_π bands are in energetic competition with the bands forming the Zhang–Rice state, if additional holes are doped. Hence, the O-2p_π orbitals must be included in the Emery model in order to correctly describe the t-terms which determine the magnetic coupling.

In $CaCuO_2$ there is a sizable dispersion of the in-plane O-$2p_\pi$ bands in z-direction mediated by some hybridization with Ca-$3d_{x^2-y^2}$ orbitals. This is in accordance with the experimental finding that $CaCuO_2$ has the highest Néel temperature, $T_N = 540$ K, of all layered cuprates indicating 3D magnetism [20,31]. For a survey of the magnetic properties of cuprates see Ref. [32].

By contrast, in $Sr_2CuO_2Cl_2$ there is no dispersion of the corresponding bands in z-direction due to the Sr_2Cl_2 buffer layers. There is only dipole–dipole coupling of the planes, compatible with the experimental findings, $T_N = 256$ K [33].

4. Conclusions

The LSDA + U approach is shown to fit perfectly in the frame of DFT by Hohenberg and Kohn for the electronic ground state, provided the theory can be closed by linking the U-value to the variational quantities, the KS orbitals and orbital occupation numbers (which explicit link is yet to be rendered). On the other hand, the LSDA + U potential is also widely understood as an approximation to the electron self-energy (first step towards an LSDA + dynamical mean-field theory). There is hope that in this way like in the situation of weakly correlated systems it provides again a tool to obtain a rather accurate ground state and a reasonable approximation to the quasi-particle spectrum (band structure) in a single run from only one set of equations. To pursue this goal, in the first part of the present paper an attempt was made to present the structure of the LSDA + U theory as clearly as possible.

Application to several typical planar cuprate structures and comparison to experimental data of the isolating electronic state and the magnetic state as well as of quasiparticle spectra probed by photoemission seems to support this expectation. On the other hand, it revealed a number of new aspects in the physics of the electronic structure of cuprates. Notably, the sufficient completeness of most model Hamiltonians in use must be questioned, at least in connection with the dimensionality and details of magnetic couplings, and the so-called bilayer splitting of the band structure of $Bi_2Sr_2CaCu_2O_8$ should be reanalyzed.

Acknowledgments

We thank H. Rosner for helpful discussions. Financial support by the German Israel Foundation under Contract No. I-614-13.14/99 and by the Deutsche Forschungsgemeinschaft, SFB 463, is gratefully acknowledged.

References

[1] P. Hohenberg, W. Kohn, Phys. Rev. 136 (1964) B864–B871; W. Kohn, L.J. Sham, Phys. Rev. 140 (1965) A1133–A1138.
[2] E.H. Lieb, Int. J. Quant. Chem. XXIV (1983) 243–277.
[3] H. Eschrig, The Fundamentals of Density Functional Theory, B.G. Teubner, Stuttgart, 1996 (a revised and extended issue is in preparation by Edition am Gutenbergplatz, Leipzig, 2003).
[4] J.F. Herbst, R.E. Watson, J.W. Wilkins, Phys. Rev. B 17 (1978) 3089–3098.
[5] P.H. Dederichs, et al., Phys. Rev. Lett. 53 (1984) 2512–2515.
[6] M.R. Norman, A.J. Freeman, Phys. Rev. B 33 (1986) 8896–8898.
[7] O. Gunnarsson, et al., Phys. Rev. B 39 (1989) 1708–1722.
[8] W.E. Pickett, C.S. Wang, Phys. Rev. B 30 (1984) 4719–4733; C.S. Wang, W.E. Pickett, Phys. Rev. Lett. 51 (1983) 597–600.
[9] M.S. Hybertsen, S.G. Louie, Phys. Rev. Lett. 55 (1985) 1418–1421.
[10] J.P. Perdew, M. Levy, Phys. Rev. Lett. 51 (1983) 1884–1887; L.J. Sham, M. Schlüter, Phys. Rev. Lett. 51 (1983) 1888–1891; W. Kohn, Phys. Rev. B 33 (1986) 4331–4333.
[11] V.I. Anisimov, J. Zaanen, O.K. Andersen, Phys. Rev. B 44 (1991) 943–954.
[12] V.I. Anisimov, et al., Phys. Rev. B 48 (16) (1993) 929–934.
[13] M.T. Czyżyk, G.A. Sawatzky, Phys. Rev. B 49 (1994) 14211–14228.
[14] V.I. Anisimov, F. Aryasetiawan, A.I. Lichtenstein, J. Phys.: Condens. Matter 9 (1997) 767–808.
[15] A.B. Shick, A.I. Liechtenstein, W.E. Pickett, Phys. Rev. B 60 (1999) 10763–10769.
[16] K. Koepernik, H. Eschrig, Phys. Rev. B 59 (1999) 1743–1757.
[17] A.I. Liechtenstein, V.I. Anisimov, J. Zaanen, Phys. Rev. B 52 (1995) R5467–R5470.
[18] Access to FPLO exists under 'http://www.ifw-dresden.de/fplo'
[19] P. Perdew, A. Zunger, Phys. Rev. B 23 (1981) 5048–5079.
[20] D. Vaknin, et al., Phys. Rev. B 39 (1989) 9122–9125.
[21] V.J. Emery, Phys. Rev. Lett. 58 (1987) 2794–2797.
[22] F.C. Zhang, T.M. Rice, Phys. Rev. B 37 (1988) 3759–3761.
[23] J.J.M. Pothuizen, et al., Phys. Rev. Lett. 78 (1997) 717–719.
[24] R. Hayn, et al., Phys. Rev. B 60 (1999) 645–658.
[25] J. Fink, et al., J. Electron Spectrosc. Relat. Phenom. 66 (1994) 395–452.
[26] L.L. Miller, et al., Phys. Rev. B 41 (1990) 1921–1925.
[27] T. Tohyama, S. Maekawa, Supercond. Sci. Technol. 13 (2000) R17–R32.
[28] A. Damascelli, Z.-X. Shen, Z. Hussain, Rev. Mod. Phys. 75 (2003) 473.
[29] F. Ronning et al., cond-mat/0209651, 2002.
[30] A.N. Yaresko, Phys. Rev. B 65 (2002) 115111-1–115111-7.
[31] R. Pozzi, et al., Phys. Rev. B 56 (1997) 759–765.
[32] D.C. Johnston, in: K.H.J. Buschow (Ed.), Handbook of Magnetic Materials, Vol. 10, Elsevier, Amsterdam, 1997, pp. 1–237 (Chapter 1).
[33] M. Greven, et al., Phys. Rev. Lett. 72 (1994) 1096–1099.